iScience

CellPress
OPEN ACCESS

Article

Design and locomotion characteristic analysis of two kinds of tensegrity hopping robots

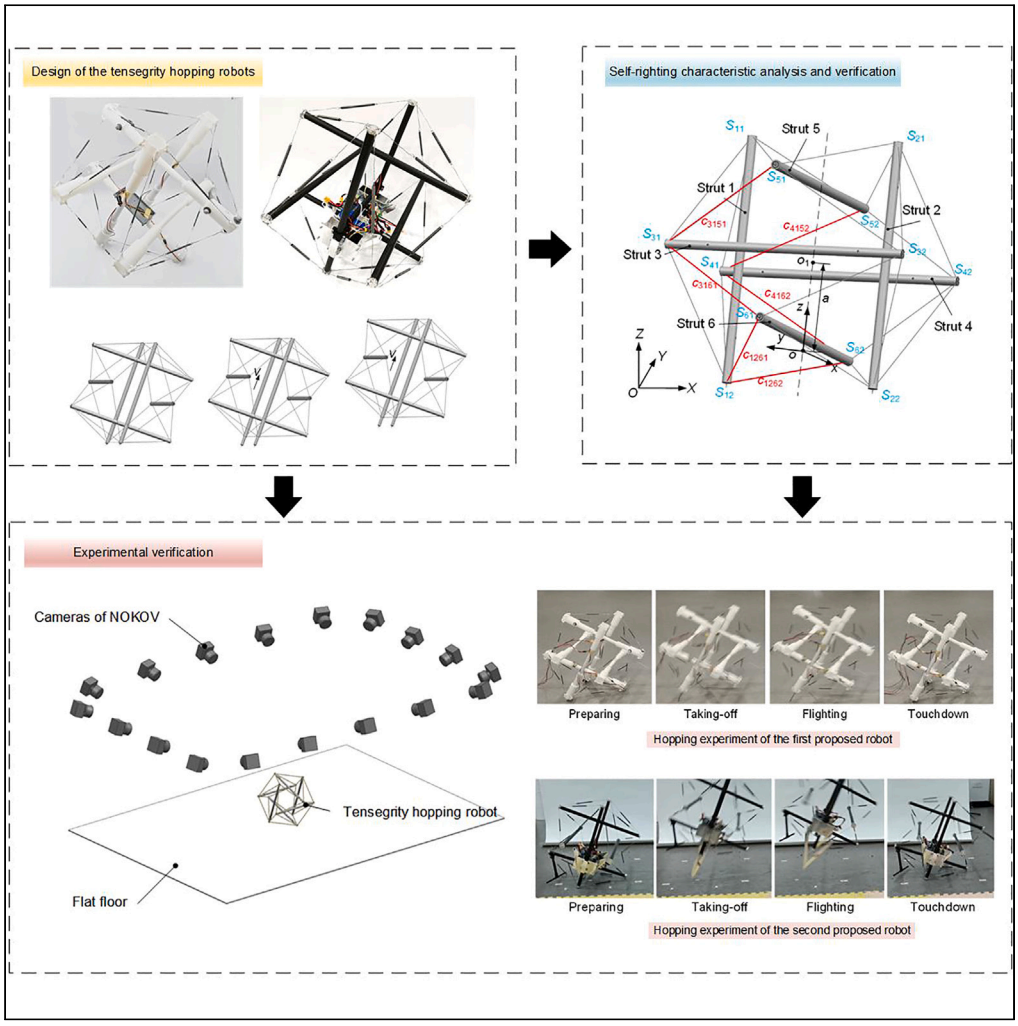

Jixue Mo, Hao Fang, Qingkai Yang

fangh@bit.edu.cn

Highlights

Two kinds of tensegrity hopping with new actuation methods robots were proposed

The self-righting characteristics were analyzed and verified by simulation

Both robots have better locomotion performance over other tensegrity robots

The proposed robots can be applied in the fields of surveillance and detection

Mo et al., iScience 27, 109226
March 15, 2024
https://doi.org/10.1016/j.isci.2024.109226

iScience

CellPress
OPEN ACCESS

Article

Design and locomotion characteristic analysis of two kinds of tensegrity hopping robots

Jixue Mo,[1] Hao Fang,[2,3,*] and Qingkai Yang[2]

SUMMARY

This study proposed two kinds of tensegrity hopping robots, which were actuated by push-pull electromagnets and servo motors, respectively. Both tensegrity robots are able to conduct stable and consecutive hopping actions. This paper covers the robots' structural designs, theoretical modeling of the hopping actuators, and detailed analysis of the robot's self-righting properties, all of which are validated by corresponding experimental and simulational results. The first hopping robot could hop forward at an average speed of 0.641 body length/s. Although the second robot has a lower moving speed of 0.237 body length/s, its average jumping height of 0.301 m is nearly 2.5 times higher than that of the first robot. Then compared with other tensegrity rolling robots, the proposed two robots show obvious advantages in locomotion performance over their counterparts. Therefore, the proposed robots can have large potential in many fields such as space exploration, urban search, military surveillance, etc.

INTRODUCTION

In recent years, the tensegrity robot, which is a novel kind of robot based on tensegrity structure, has drawn the interest of lots of researchers. Tensegrity structure usually refers to a structure composed of non-continuous rigid struts connected by a continuous net of tensile flexible cables.[1] Different from cable-driven structures or serial-parallel hybrid structures,[2,3] the tensegrity structure has no direct contact between rigid struts.[4] Once suffering from the external load, the structure's struts and cables would undergo compressive forces and tensile forces, respectively, hence determining the structure's overall shape. Compared with traditional rigid structures, the tensegrity structure has various characteristics, including high flexibility, high adaptability, tunable stiffness, superior strength-to-mass ratios, high redundancy, excellent actuation efficiency, and global force distribution.[5,6] These distinctive features and advantages make the tensegrity structure an indispensable and valuable research object.

In the last few decades, various tensegrity robots have been developed by different researchers. The seminal research work by Paul and Lipson of Cornell University in 2006 made the concept of tensegrity robot widely spread across the world.[7] The modular tensegrity robot inspired by natural organisms, Tensegripede, was able to cross obstacles nearly the same size of its own wheel.[8] Saitanay et al. designed a topologically tensegrity spine structure; it could perform cartwheel movements to go across unfamiliar terrains.[9] It is worth noting that NASA ushered in the application of tensegrity robots in space exploration. They developed the SUPERball, a spherical tensegrity robot distinguished by its good locomotion and shock-absorption abilities, making it suitable for being deployed in most high-altitude environments and unstructured terrains.[10–12] Therefore, it can be a good substitute for conventional wheeled robots due to its lightweight and low price. In cooperation with NASA, the researchers of University of California (UC) Berkeley developed a series of 6-bar spherical tensegrity robots, which can conduct stable rolling movements actuated by motors and cables.[13,14]

Nonetheless, the most common locomotion modality for tensegrity robots is cable-driven rolling movement. This often leads to undesirable locomotion speeds and zigzag moving trajectories, and the control methods of cable-driven rolling are often complex, thereby affecting their locomotion efficiencies negatively. On the other hand, jumping robots or hopping robots often have remarkable locomotive capabilities; they can easily overcome obstacles several times larger than their own dimensions. Jumping motions can be realized in various ways, such as combustion-driven jumping, spring and motor-driven jumping, or air cylinder-driven jumping. It is noteworthy that Raibert first designed a series of single-legged, bipedal, and quadrupedal jumping robots based on the spring-inverted pendulum model.[15] The Sandflea jumping robot of Boston Dynamics, actuated by an explosive cylinder, could achieve a remarkable height of almost 10 m and was able to conduct 25 consecutive jumps at most with adjustable jump height and distance.[16] In addition, researchers at Seoul National University devised a flea-inspired jumping robot, weighing merely 1.1 g and measuring nearly 2 cm in size.[17,18] This robot could imitate the cooperative working mechanism of the biotic flea's hind leg muscles, enabling it to achieve jumping height nearly 30 times its own size. Thus it is quite meaningful to empower jumping capability for tensegrity robots so that their mobilities in unstructured environments and practical applicability can be significantly improved.

[1]Department of Strategic and Advanced Interdisciplinary Research, Peng Cheng Laboratory, Shenzhen 518055, China
[2]Key Laboratory of Intelligent Control and Decision of Complex Systems, Beijing 100081, China
[3]Lead contact
*Correspondence: fangh@bit.edu.cn
https://doi.org/10.1016/j.isci.2024.109226

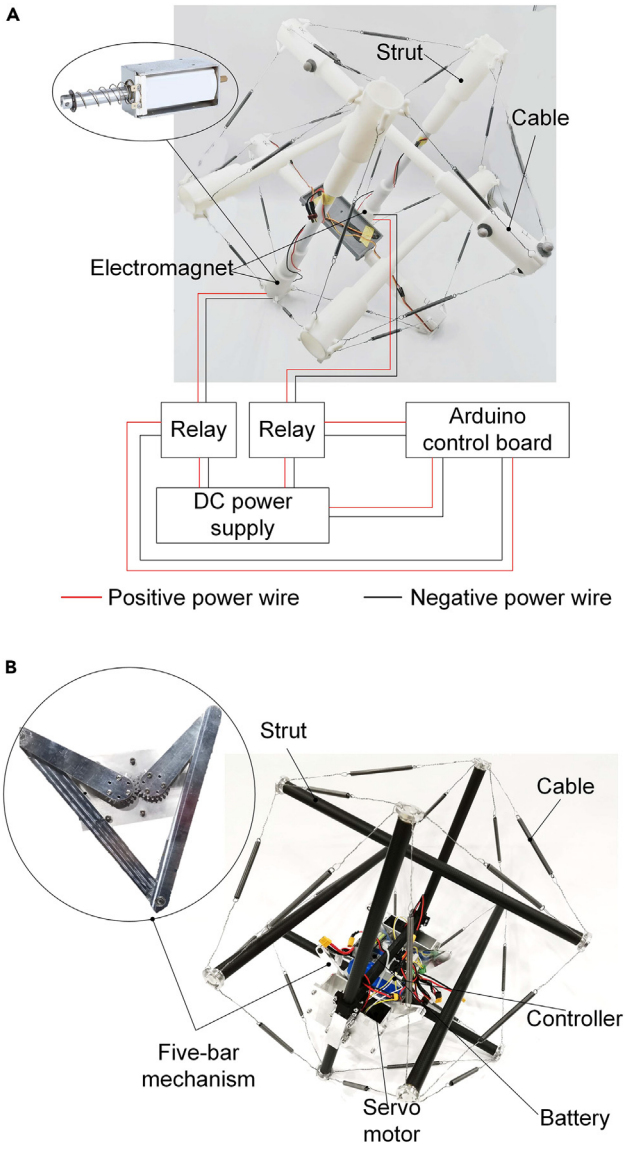

Figure 1. Two tensegrity hopping robot prototypes
(A) The tensegrity hopping robot driven by electromagnets.
(B) The tensegrity hopping robot driven by 5-bar mechanisms.

This paper proposed two novel tensegrity hopping robots, which were driven by electromagnets and servo motors, respectively. Both robots were featured with better locomotion ability and self-righting characteristics compared with other conventional tensegrity mobile robots. Firstly, the structural design and working principles of the proposed robots were illustrated in detail. Then the mathematical models of two kinds of hopping actuators and single hopping process were presented in sequence. In addition, a detailed analysis of the robots' self-righting properties was also conducted, and its theoretical results were verified by a series of motion simulations. Finally, real-world experiments validated the good hopping and progressing abilities of the two tensegrity hopping robots, affirming their superior locomotion capabilities compared with conventional tensegrity mobile robots.

Design and configuration

Structural design

Figures 1A and 1B illustrate two different tensegrity hopping robot schemes, respectively. As shown in Figure 1A, the first tensegrity hopping robot is mainly comprised of a 6-strut spherical tensegrity structure, two electromagnets, two relays, an off-board 24V DC power supply and a control board. Notably, the tensegrity structure has 6 struts and 24 cables, and each strut and cable sustain compression and tension

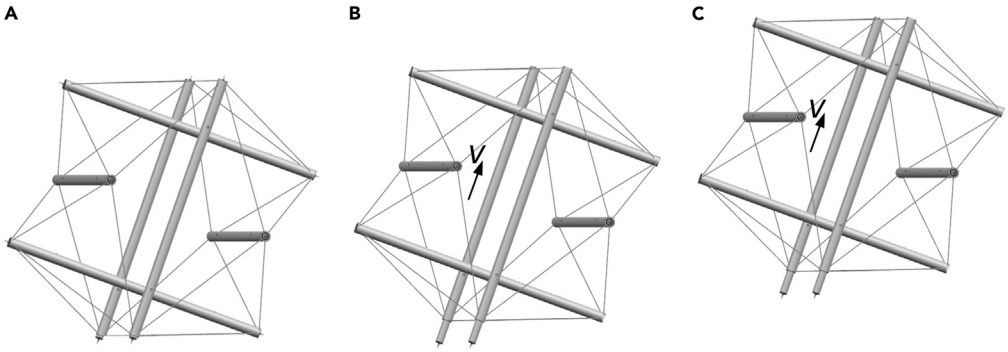

Figure 2. Working process of the tensegrity hopping robot
(A) Preparing stage.
(B) Take-off stage.
(C) Flight stage.

respectively. Then the two electromagnets are mounted on the same end of one pair of parallel struts, so as to enable the robot's jumping movement. Additionally, the control board (Arduino UNO) is applied to control the actuation characteristics of electromagnets with relays and thus implement the robot's progressing and steering movement.

In terms of the second tensegrity hopping robot, as presented in Figure 1B, its main difference from the first robot is that it takes a pair of servo motor driven 5-bar mechanism as the jumping actuator. In addition, it also contains an onboard 48V DC power supply and a control board based on the STM32 platform, which controls the servo motor's force output performance and realizes progressing and steering movement.

Working process

Both jumping actuators, either push-pull electromagnets or servo motor driven 5-bar mechanism, can have rapid responsiveness in force outputting and reliable structure, hence they are suitable to be actuators of the proposed tensegrity hopping robot. Therefore, as shown in Figure 2, the single jumping process can be divided into three stages.

(1) Preparing stage. The robot adjusts itself to the state that both jumping actuators contact with the ground by its gravitational torque (Figure 2A);
(2) Take-off stage. The robot accelerates upwards in a short time by enabling the two jumping actuators with specific driving parameters (Figure 2B);
(3) Flight stage. The robot keeps moving upwards to the maximum height and then falls freely to the ground again under gravity ((Figure 2C).

So the robot can achieve consecutive jumping movements by repeating the aforementioned single jumping process, and its steering angle while progressing can also be adjusted by applying different driving parameters for the left and right jumping actuators.

Working parameters

For the first robot, its tensegrity structure is mainly composed of 6 struts and 24 cables. Notably, each cable contains an extension spring with an elastic coefficient of 1109.7 N/mm. Thus the lengths of struts and stretched cables are 521.8 mm and 323.1 mm, respectively. For a lightweight design, each strut was made of 3D-printed resin, realizing a final weight of 0.129 kg. In addition, the driving voltage of the electromagnet can range from 15 V to 30 V (DC), which also corresponds to different force-outputting performances.

In terms of the second robot, its overall dimension is close to the first one, and its cables' elastic coefficient is the same as the first one (1109.7 N/m). It is noteworthy that the driving voltage of the second robot's servo motor is 48V DC, while the driving current can be adjusted in the range of 0∼10 A by the MC6030 control board, thus determining its torque output performance. Therefore, the configuration information of two proposed robots can be seen from Table 1 in detail.

Modeling and self-righting analysis

Mathematical model of push-pull electromagnet

The first tensegrity hopping robot was driven by a pair of push-pull electromagnets and the generated electromagnetic attraction force of solenoid electromagnet can be generally calculated by:

$$F_m = \frac{(NI)^2 \mu_0}{2\delta^2} S \qquad \text{(Equation 1)}$$

Table 1. Robot's configuration and working parameters

Parameter name	Configuration of the first robot	Configuration of the second robot
Overall weight	2.42 kg	4.21 kg
Overall dimension	521.8 × 521.8 × 521.8 mm	502.5 × 502.5 × 502.5 mm
Length of strut	521.8 mm	502.5 mm
Length of stretched cable	323.1 mm	304.6 mm
Weight of struts	0.129 kg × 6	0.133 kg × 6
Weight of cables	0.019 kg × 24	0.027 kg × 24
Weight of jumping actuators	0.598 kg × 2	1.012 kg × 2
Driving Voltage	15V–30 V DC	48V DC

where N is turns per coil, I is current intensity (A), μ_0 is the permeability of vacuum ($4\pi\times10^{-7}$ Wb/A•m), S is the cross-sectional area of magnetic circuit (m^2) and δ is gas length (mm).[19] It can be seen from Equation 1 that F_m is directly proportional to the turns per coil N, the square of current intensity I^2, the cross-sectional area of magnetic circuit S, while inversely proportional to the square of gas length δ^2.

Then the generated acceleration a of the armature pusher and its payload is:

$$a = \frac{F_m - M_{tot}g}{M_{tot}} \quad \text{(Equation 2)}$$

where M_{tot} is the total mass of the armature pusher and its payload.

Hence thrust process of the electromagnet can be recorded by a motion capture system, and the experimental displacement curve of the loaded armature can be obtained. Then by comparing the experimental curve and the corresponding theoretical curve, the specific relationship between the armature's performance characteristics and its influence factors would be confirmed, thus providing a fundamental basis for further experiments.

Mathematical model of 5-bar mechanism

The jumping actuators of the second hopping robot are a pair of servo motor-driven geared 5-bar mechanisms. Figure 3 illustrates the schematic diagram of the geared 5-bar mechanisms. It is noteworthy that the link L_{AC} and link L_{BD} are fixed with the active gear and the passive gear, respectively. Thus the degree of freedom of the applied geared 5-bar mechanism is 1.

By analyzing the geometrical relationship of the geared 5-bar mechanism, it can be obtained that:

$$\begin{cases} a\sin\alpha + b\sin\beta = y_E \\ a\cos\alpha = b\cos\beta + c/2 \end{cases} \quad \text{(Equation 3)}$$

where a, b, and c are the length of link L_{CE}, L_{AC}, and L_{AB}, respectively; α and β are the horizontal angles of link L_{CE} and L_{AC}, respectively; y_E is the displacement of E along y axis.

Then the expressions of α and β can be attained by transforming (3):

$$\begin{cases} \alpha = \arcsin(\lambda/\rho) - \varphi \\ \beta = \arcsin[(y_E - a\sin\alpha)/b] \end{cases} \quad \text{(Equation 4)}$$

where λ, ρ, and φ are intermediate variables:

$$\begin{cases} \lambda = \left(y_E^2 + c^2 \middle/ 4 + a^2 - b^2\right) \middle/ a \\ \rho = \sqrt{4y_E^2 + c^2} \\ \varphi = \arcsin(c/\rho) \end{cases} \quad \text{(Equation 5)}$$

To simplify the calculation, it can be supposed that all links only suffer forces in their ends and the suffered forces of link L_{AC} and link L_{BD} are F_a and F_b respectively. Assuming the servo motor's output torque is M_0, then M_0 can be equivalent to driving forces F_0 acting on points C and D. Therefore, the following equations can be obtained:

$$\begin{cases} F_a\cos\alpha + F_b\cos\beta = F_0 \\ 2F_a\sin\alpha = F_y \\ 2F_b\sin\beta = F_y \\ F_0 = \dfrac{M_0}{2b\sin\beta} \end{cases} \quad \text{(Equation 6)}$$

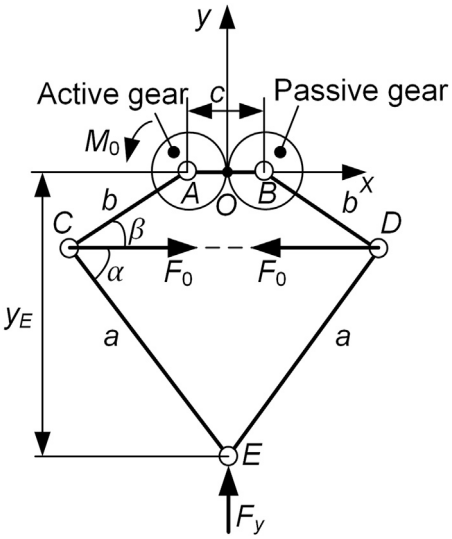

Figure 3. Schematic diagram of the geared 5-bar mechanism

Eliminating F_a and F_b, the relationship between F_y and y_E can be obtained as:

$$F_y = \frac{M_0}{b \sin\beta\left(\frac{1}{\tan\alpha}+\frac{1}{\tan\beta}\right)} \quad \text{(Equation 7)}$$

Therefore, the impulse acting on the 5-bar mechanism can be calculated by Equation 7, and the final velocity of the take-off stage for a single hopping process can also be obtained according to the theorem of momentum.

Mathematical model of the hopping process

Firstly, there is a supposition that the cables' elastic coefficient of the tensegrity structure is large enough so that the effect of internal forces of tensegrity structure on its locomotion characteristics can be ignored; additionally, the spherical tensegrity structure can be seen as a regular icosahedron. Thus it is noteworthy that the center of mass of the tensegrity robot is located just under its geometric center because of the mounting positions of the electromagnets.

As shown in Figure 4, the ground coordinate system *OXZY* and body coordinate system *oxyz* can be built with the robot's center of gravity being the origin *o*. The *x* axis and *z* axis are parallel with strut 6 and strut 1, respectively. Then $\boldsymbol{F_1}$ and $\boldsymbol{F_2}$ denote the thrust acting on strut 1 and strut 2 by the two electromagnets, respectively.

The robot's general rotational kinetic equation can be written as:

$$M\dot{v}^e = \left(F_1^b + F_2^b\right) - G^e \quad \text{(Equation 8)}$$

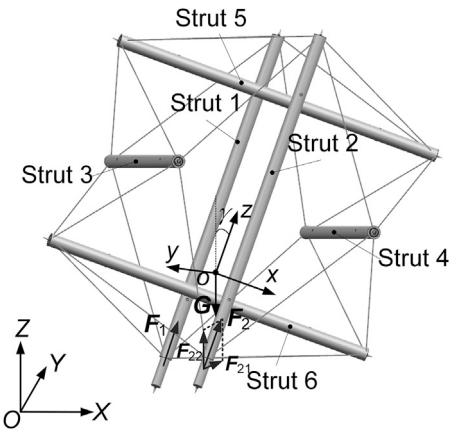

Figure 4. Schematic diagram of tensegrity robot's coordinate systems

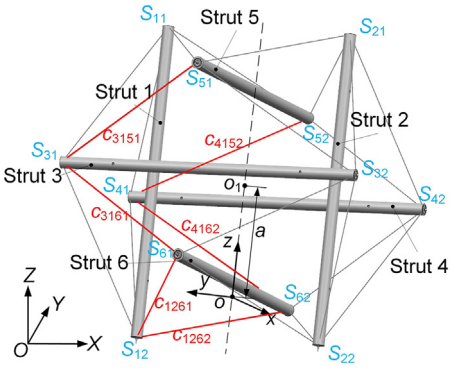

Figure 5. The schematic diagram of tensegrity robot's self-righting analysis

where M is the total weight of the tensegrity robot, $\boldsymbol{G}$ is the gravity. The subscripts b and e represent the vectors of coordinate system $OXYZ$ and $oxyz$ respectively.

Integrating (Equation 8) with the rotation matrix from coordinate system $oxyz$ to $OXYZ$, the robot's center-of-mass velocity components can be obtained as:

$$\begin{cases} \dot{v}_x^e = \dfrac{f_1+f_2}{M}(\cos\psi\sin\theta\cos\varphi+\sin\psi\sin\varphi) \\ \dot{v}_y^e = \dfrac{f_1+f_2}{M}(\sin\psi\sin\theta\cos\varphi-\cos\psi\sin\varphi) \\ \dot{v}_z^e = \dfrac{f_1+f_2}{M}\cos\varphi\cos\theta-g \end{cases} \quad \text{(Equation 9)}$$

where f_1 and f_2 are the magnitudes of thrust $\boldsymbol{F_1}$ and $\boldsymbol{F_2}$; φ, θ, ψ are the Euler angles about axis x, y, z, respectively.

On the other hand, the rotational kinetic equation of the robot can be represented as:

$$I\dot{\boldsymbol{\omega}}^b+\boldsymbol{\omega}^b\times J\boldsymbol{\omega}^b=\boldsymbol{\tau} \quad \text{(Equation 10)}$$

where $\boldsymbol{\omega}^b$ is the robot's angular velocity in the coordinate system $oxyz$ and p, q, r are its three components; J is the moment of inertia relative to the robot's center of mass; $\boldsymbol{\tau}$ is the generated torque by $\boldsymbol{F_1}$ and $\boldsymbol{F_2}$ in coordinate system $oxyz$.

The proposed tensegrity robot is symmetric about plane xoz and yoz, while asymmetric about plane xoy. So the robot's inertial matrix can be written as:

$$I=\begin{bmatrix} I_{xx} & I_{xy} & \\ I_{yx} & I_{yy} & \\ & & I_{zz} \end{bmatrix} \quad \text{(Equation 11)}$$

Substituting (Equation 11) into (Equation 10), the three components of $\boldsymbol{\omega}^b$ can be attained as:

$$\begin{cases} \dot{p} = \dfrac{I_{yy}P-I_{xy}Q}{I_{xx}I_{yy}-I_{xy}^2} \\ \dot{q} = \dfrac{I_{xy}P-I_{xx}Q}{I_{xy}^2-I_{xx}I_{yy}} \\ \dot{r} = \dfrac{R}{I_{zz}} \end{cases} \quad \text{(Equation 12)}$$

Table 2. Coordinates of all strut ends

Strut's endpoint	Coordinate	Strut's endpoint	Coordinate
S_{11}	(0, l_1/2, l_0/2+a)	S_{41}	(l_1/2, l_0/2, a)
S_{12}	(0, l_1/2, -l_0/2+a)	S_{42}	(l_1/2, -l_0/2, a)
S_{21}	(0, -l_1/2, l_0/2+a)	S_{51}	(-l_0/2, 0, l_1/2+a)
S_{22}	(0, -l_1/2, -l_0/2+a)	S_{52}	(l_0/2, 0, l_1/2+a)
S_{31}	(-l_1/2, l_0/2, a)	S_{61}	(-l_0/2, 0, -l_1/2+a)
S_{32}	(-l_1/2, -l_0/2, a)	S_{62}	(l_0/2, 0, -l_1/2+a)

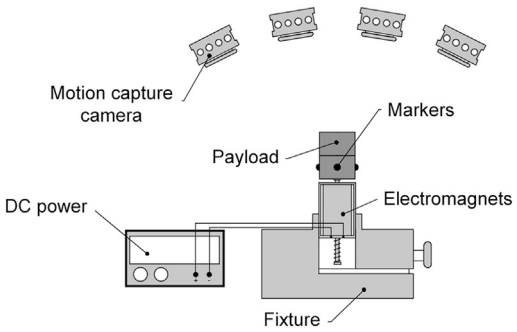

Figure 6. The experimental setup of electromagnet's thrust test

where the variables of P, Q, and R are:

$$\begin{cases} P = \tau_x - I_{zz}qr + I_{xy}\,pr + I_{yy}qr \\ Q = \tau_y - I_{xx}qr - I_{xy}qr + I_{zz}\,pr \\ R = \tau_z - I_{xy}p^2 - I_{yy}pq + I_{xx}pq + I_{xy}q^2 \end{cases} \quad \text{(Equation 13)}$$

When the robot only suffers minor disturbance, the rangeability of Euler angles is not large. Thus it can be assumed that the changing rate of Euler angles is approximate to the body angular velocities, and the robot's nonlinear six-degree kinetic equations while hopping are:

$$\begin{cases} \ddot{x} = \dfrac{f_1+f_2}{M}(\cos\psi\sin\theta\cos\varphi + \sin\psi\sin\varphi) \\ \ddot{y} = \dfrac{f_1+f_2}{M}(\sin\psi\sin\theta\cos\varphi - \cos\psi\sin\varphi) \\ \ddot{z} = \dfrac{f_1+f_2}{M}\cos\varphi\cos\theta - g \\ \ddot{\varphi} = \dfrac{I_{yy}P - I_{xy}Q}{I_{xx}I_{yy} - I_{xy}^2} \\ \ddot{\theta} = \dfrac{I_{xy}P - I_{xx}Q}{I_{xy}^2 - I_{xx}I_{yy}} \\ \ddot{\psi} = \dfrac{R}{I_{zz}} \end{cases} \quad \text{(Equation 14)}$$

Self-righting analysis

It is worth noting that the aforementioned hopping actuators, either electromagnets or 5-bar mechanism, are mounted on similar positions of the tensegrity structure. Thus for simplification, only the first robot structural scheme is analyzed in this part. As shown in Figure 5, the robot takes $\Delta S_{12}S_{22}S_{62}$ as the initial grounded triangle for hopping when its center of mass is located just beneath its geometric center. Then after a single hopping and landing movement, the robot can revert to the state in which the base triangle ($\Delta S_{12}S_{22}S_{62}$ or $\Delta S_{12}S_{22}S_{61}$) is always the grounded triangle with high probability. This is the robot's self-righting characteristics and it's indispensable for the robot's consecutive hopping movement.

Table 3. The experimental results of thrust test of electromagnet

No.	Payload Mass (kg)	Driving voltage (V)	Duration of action (s)	Max velocity (m/s)	Max Accelaration (m/s^2)
1	0.6159	22.0	0.093	1.771	334.290
2		23.0	0.086	1.888	380.698
3		24.0	0.081	1.907	427.075
4		25.0	0.074	2.047	461.218
5	1.0903	22.0	0.160	1.335	205.392
6		23.0	0.141	1.415	269.522
7		24.0	0.119	1.468	305.193
8		25.0	0.099	1.532	357.807

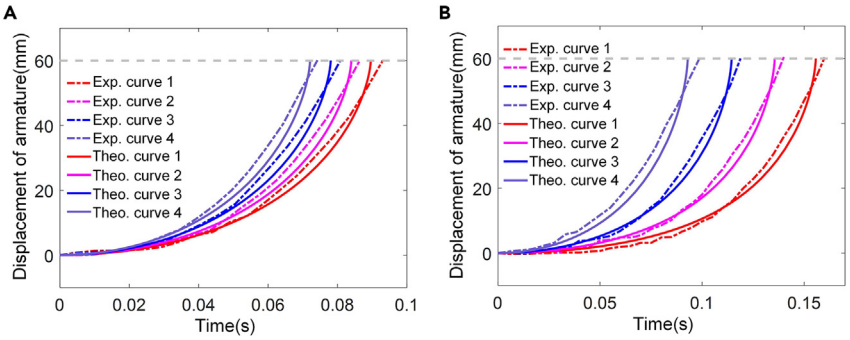

Figure 7. Displacement curves of electromagnet's armature

(A) Displacement curves of 0.6159 kg payload.

(B) Displacement curves of 1.0903 kg payload.

The applied spherical tensegrity structure can be treated as a regular icosahedron. It is noteworthy that there are 14 triangles having self-righting functions among all 20 triangles except $\Delta S_{11}S_{31}S_{41}$, $\Delta S_{12}S_{31}S_{41}$, $\Delta S_{11}S_{21}S_{51}$, $\Delta S_{11}S_{21}S_{52}$, $\Delta S_{22}S_{32}S_{42}$, and $\Delta S_{21}S_{32}S_{42}$. As the tensegrity structure is symmetric about plane *xoz*, its left part along plane *xoz* can be analyzed as an example. Assuming the offset distance of robot's center of mass is *a*, then the coordinates of robot's geometric center o_1 is (0, 0, *a*). So the coordinates of all strut ends can be listed in Table 2, which can further be used to calculate the vectors of all strut ends.

Subsequently, the projection point coordinate *o'* on different triangle planes can be calculated, thus determining the critical condition of self-righting in each case. Taking the initial grounded triangle of $\Delta S_{12}S_{41}S_{62}$ as an example, the robot aims to roll around edge c_{1262} and revert to the state with $\Delta S_{12}S_{22}S_{62}$ being the final grounded triangle.

Supposing the normal vector of $\Delta S_{12}S_{41}S_{62}$ is $\boldsymbol{n}_1 = (n_{1x}, n_{1y}, n_{1z})$, then its three components can be calculated by the cross product operation of points S_{12} (S_{12x},S_{12y}, S_{12z}), S_{41} (S_{41x}, S_{41y}, S_{41z}), and S_{62} (S_{62x}, S_{62y}, S_{62z}), namely:

$$\begin{cases} n_{1x} = (S_{41y} - S_{12y})(S_{62z} - S_{12z}) - (S_{62y} - S_{12y})(S_{41z} - S_{12z}) \\ n_{1y} = (S_{62x} - S_{12x})(S_{41z} - S_{12z}) - (S_{41x} - S_{12x})(S_{62z} - S_{12z}) \\ n_{1z} = (S_{41x} - S_{12x})(S_{62y} - S_{12y}) - (S_{62x} - S_{12x})(S_{41y} - S_{12y}) \end{cases} \quad \text{(Equation 15)}$$

Then the components of the projection point *o'* (o'_x, o'_y, o'_z) on plane $\Delta S_{12}S_{41}S_{62}$ generated by *o*(0, 0, 0) are:

$$\begin{cases} o'_x = n_{1x}\dfrac{n_{1x}S_{12x}+n_{1y}S_{12y}+n_{1z}S_{12z}}{n_{1x}^2+n_{1y}^2+n_{1z}^2} \\ o'_y = n_{1y}\dfrac{n_{1x}S_{12x}+n_{1y}S_{12y}+n_{1z}S_{12z}}{n_{1x}^2+n_{1y}^2+n_{1z}^2} \\ o'_z = n_{1z}\dfrac{n_{1x}S_{12x}+n_{1y}S_{12y}+n_{1z}S_{12z}}{n_{1x}^2+n_{1y}^2+n_{1z}^2} \end{cases} \quad \text{(Equation 16)}$$

In addition, the equation of edge c_{1262} can also be attained as:

$$\frac{x - S_{12x}}{S_{62x} - S_{12x}} = \frac{y - S_{12y}}{S_{62y} - S_{12y}} = \frac{z - S_{12z}}{S_{62z} - S_{12z}} \quad \text{(Equation 17)}$$

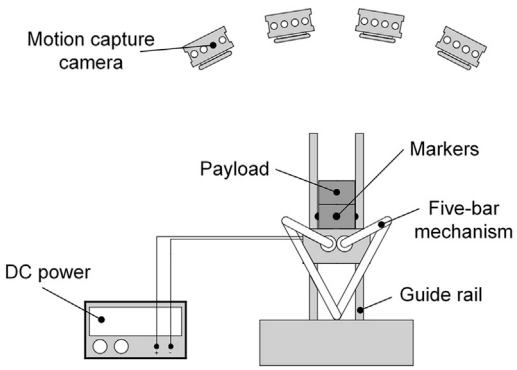

Figure 8. The experimental setup of 5-bar mechanism's thrust test

Table 4. Experimental results of thrust test of 5-bar mechanism

No.	Payload mass (kg)	Driving current (A)	Duration of action (s)	Max velocity (m/s)	Max accelaration (m/s^2)
1	0.6159	3.0	0.142	1.901	57.339
2		4.0	0.114	2.493	79.883
3		5.0	0.097	3.018	106.416
4		6.0	0.082	3.605	143.679
5	1.0903	3.0	0.188	1.345	41.776
6		4.0	0.140	1.946	62.483
7		5.0	0.116	2.429	83.511
8		6.0	0.098	2.955	111.517

It can be seen that the distance $d_{o'c1}$ between o' and c_{1262} would decrease and then increase with the value of a increases. Thus the robot would reach the critical state of self-righting characteristic when o' locates on the edge c_{1262}, that is $d_{o'c1} = 0$ and $a = a_{crt1}$. It means the robot can perform self-righting when $a > a_{crt1}$. Supposing $\boldsymbol{l}_{o'c1}$ is the vector from o' to any point on c_{1262}, $\boldsymbol{\tau}_1$ is the direction vector of edge c_{1262}, thus $d_{o'c1}$ can be calculated by:

$$d_{o'c1} = \frac{\left|\boldsymbol{l}_{o'c_1} \times \boldsymbol{\tau}_1\right|}{\left|\boldsymbol{\tau}_1\right|} \quad \text{(Equation 18)}$$

Then the value of a_{crt1} can be attained according to (Equations 15–18), that is:

$$a_{crt1} = \underset{a}{\operatorname{argmin}} d_{o'c1} \quad \text{(Equation 19)}$$

The computational methods of a_{crt2} and a_{crt3} are similar to that of the value of a_{crt1}, which are calculated according to (Equations 18 and 19). a_{crt1}, a_{crt2}, and a_{crt3} corresponds to the first adjacent triangles ($\Delta S_{12}S_{41}S_{62}$ and $\Delta S_{12}S_{31}S_{61}$), the second adjacent triangles ($\Delta S_{41}S_{52}S_{62}$ and $\Delta S_{31}S_{51}S_{61}$), and the third adjacent triangles ($\Delta S_{11}S_{41}S_{52}$ and $\Delta S_{31}S_{11}S_{51}$) of the base triangles ($\Delta S_{12}S_{22}S_{62}$ and $\Delta S_{12}S_{22}S_{61}$), respectively. Thus the values of a_{crt1}, a_{crt2}, and a_{crt3} can be calculated to be 0.123 m, 0.108 m, and 0.144 m, respectively. It is worth noting that there is always the case that $d_{o'c2} > d_{o'c1} > d_{o'c3}$ when a takes the same value and $a > 0.144$ m. Therefore it can be supposed that the robot has the smallest self-righting torque when the initial grounded triangles are the third adjacent triangles ($\Delta S_{11}S_{41}S_{52}$ and $\Delta S_{31}S_{11}S_{51}$). Hence the robot would have the highest probability of successful self-righting when the robot's actual offset distance $a > a_{crt3}$.

Additionally, as each cable of the robot is light enough relative to the struts or electromagnet, its effect on the robot's center of mass can be dismissed. It can be assumed that the mass of each strut and electromagnet is m_1 and m_2, respectively, and the position vectors of each strut and electromagnet are $\boldsymbol{r}_{1i}$ (i = 1, 2, 3, 4, 5, 6) and $\boldsymbol{r}_{2j}$ (j = 1, 2), respectively. Then the coordinate of o_1 in the body coordinate system would be

$$\begin{cases} x_{o_1} = \dfrac{m_1 \sum_{i=1}^{6} x_{1i} + m_2 \sum_{j=1}^{2} x_{2j}}{6m_1 + 2m_2} \\ y_{o_1} = \dfrac{m_1 \sum_{i=1}^{6} y_{1i} + m_2 \sum_{j=1}^{2} y_{2j}}{6m_1 + 2m_2} \\ z_{o_1} = \dfrac{m_1 \sum_{i=1}^{6} z_{1i} + m_2 \sum_{j=1}^{2} z_{2j}}{6m_1 + 2m_2} \end{cases} \quad \text{(Equation 20)}$$

where x_{1i}, y_{1i}, z_{1i} and x_{2j}, y_{2j}, z_{2j} are the three components of $\boldsymbol{r}_{1i}$ and $\boldsymbol{r}_{2j}$, respectively. Therefore the relationship between the offset distance of the robot's center of mass a, the electromagnet's mass, and mounting position can be determined by Equation 20, which isfollowed by determining the values of m_2 and $\boldsymbol{r}_{2j}$.

RESULTS AND DISCUSSION

Experiment of the electromagnet

The experiment of electromagnet is meant to test its thrust performance with payload and verify the reasonability of Equation 1 established in the last part. Figure 6 shows experimental setup of the electromagnet's thrust test. The payload consists of 1∼2 steel mass block, the mass of single mass block and the armature are 0.4744 kg and 0.1415 kg, respectively. Besides, the values of turns per coil N, cross-sectional area of

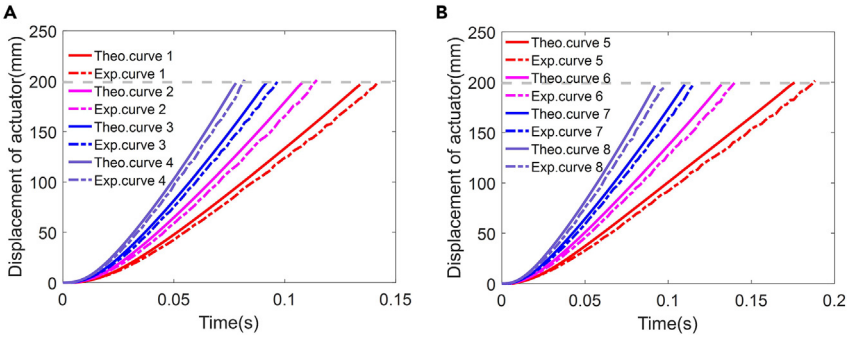

Figure 9. Displacement curves of 5-bar mechanism

(A) Displacement curves of 0.6159 kg payload.

(B) Displacement curves of 1.0903 kg payload.

magnetic circuit S and maximum gas length δ_{max} are 845, 176.71 mm^2 and 60 mm, respectively. The armature's movement was recorded by the NOKOV motion capture system with a sampling frequency of 200 Hz.

Thus the experimental results and armature's displacement curves were presented in Table 3 and Figure 7. It can be observed from Figure 7 that the duration of action becomes smaller with the increase of driving voltage, and the action velocity also becomes larger as the armature's traveling distance increases. Additionally, it can be seen that the armature's maximum velocity and acceleration become larger with the increase of driving voltage according to Table 3. Then the maximum value and average value of MAPE (mean absolute percentage error) for Figure 7 are 13.40% and 11.02%, respectively. So it is believed that the theoretical displacement curves basically conform with the experimental curves, thus verifying the reasonability of Equation 1.

Experiment of 5-bar mechanism

Similarly, the experiment of the 5-bar mechanism aimed to measure its thrust property and validate the rationality of Equation 7 proposed in the last part. Figure 8 shows the experimental setup of the 5-bar mechanism's thrust test. The applied mass block payload was kept the same with the experiment of the electromagnet, and the mass of the 5-bar mechanism is 1.012 kg. In addition, the 5-bar mechanism's movement was also recorded by NOKOV with the same sampling frequency of 200 Hz.

It is noteworthy that the corresponding relationship between output torque and driving current of the servo motor can be determined by referencing its technical manual. According to the experimental results presented in Table 4 and Figure 9, the actuation duration was also reduced with the enhancement of the driving current. The velocity of the 5-bar mechanism surges up initially and then tends to be stable until the end of the actuation. Then the maximum value and average value of MAPE for Figure 9 are 12.23% and 9.87% respectively. Hence it can be assumed that the theoretical displacement curves are basically in accord with their experimental counterparts, thus validating the rationality of Equation 7.

Self-righting simulation

After analyzing the robot's self-righting characteristic theoretically, its calculation results can be verified by UG NX 9.0 software. Table 5 lists the robot's self-righting details after free falling from 1.0 m height under 49 different cases, in which "1" represents the grounded triangle as one of the base triangles while "0" represents the opposite. Figure 10 illustrates the motion simulation setup of the robot's self-righting

Table 5. Details of the robot's self-righting simulation

		Offset distance of the robot's center of mass *a*						
Initial fall attitude angle		0.085m	0.100m	0.115m	0.130m	0.145m	0.160m	0.175m
Case 1	Roll = −60.3757°, Pitch = 129.594°,Yaw = −136.697°	0	0	0	0	1	1	1
Case 2	Roll = 23.1448°,Pitch = 20.2652°, Yaw = −19.2248°	0	1	0	1	1	1	1
Case 3	Roll = −52.8048°,Pitch = 157.6349°, Yaw = 113.6814°	0	0	1	0	1	1	1
Case 4	Roll = −14.4437°,Pitch = 43.4021°, Yaw = −58.8314°	0	0	1	1	1	1	1
Case 5	Roll = −45.5693°,Pitch = 3.4283°, Yaw = −159.5250°	1	1	0	1	1	1	1
Case 6	Roll = °-27.4856°,Pitch = 12.0787°, Yaw = −137.7686°	0	0	0	1	1	1	1
Case 7	Roll = −47.428°,Pitch = 166.7418°, Yaw = −169.2543°	0	1	1	0	1	1	1

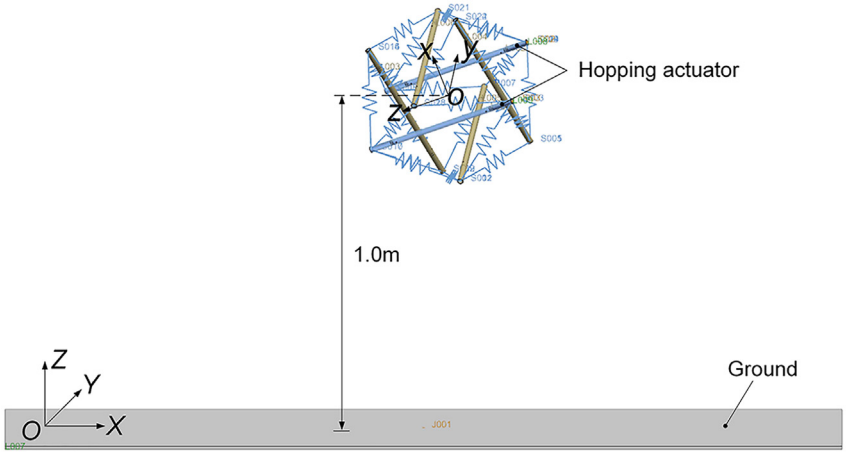

Figure 10. The simulation setup of robot's self-righting analysis

analysis and Figure 11 presents the curve graphs of the angle between the base triangle's normal vector and the ground's normal vector in 0 ~ 4s after the robot's landing movement. Figures 11A–11D correspond to case 1, case 3, case 5, and case 7 respectively. It is noteworthy that the base triangles refer to $\Delta S_{12}S_{22}S_{61}$ and $\Delta S_{12}S_{22}S_{62}$. Thus the plotted angle curves would be of the specific base triangle which finally contacts the ground after the robot's landing. If the grounded triangle was not one of the base triangles, then the angle curve of $\Delta S_{12}S_{22}S_{61}$ would be plotted.

It can be determined from Table 5 that the robot can always revert to the state in which the grounded triangle is the base triangle with 7 different initial falling attitude angles when a is larger than its critical value a_{crt3} of 0.144 m. However, when $a < a_{crt3}$, the number of robot's successful self-righting gradually becomes smaller as a decreases. Thus the failure rate for all cases of $a < a_{crt3}$ and $a > a_{crt3}$ are 60.7% and 0,

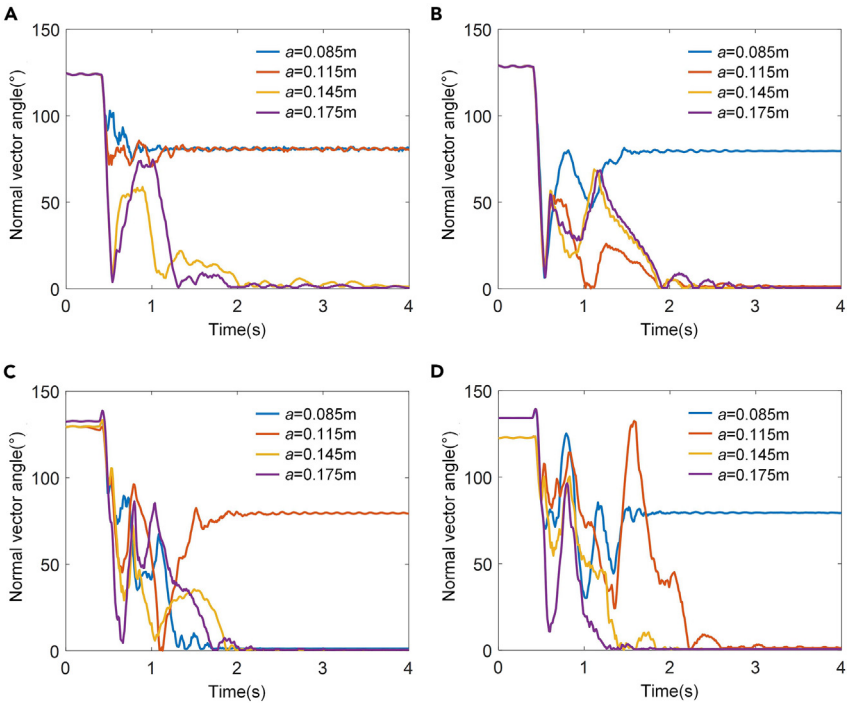

Figure 11. The angle curves of base triangle's normal vector after landing

(A) Normal vector angle in case 1.
(B) Normal vector angle in case 3.
(C) Normal vector angle in case 5.
(D) Normal vector angle in case 7.

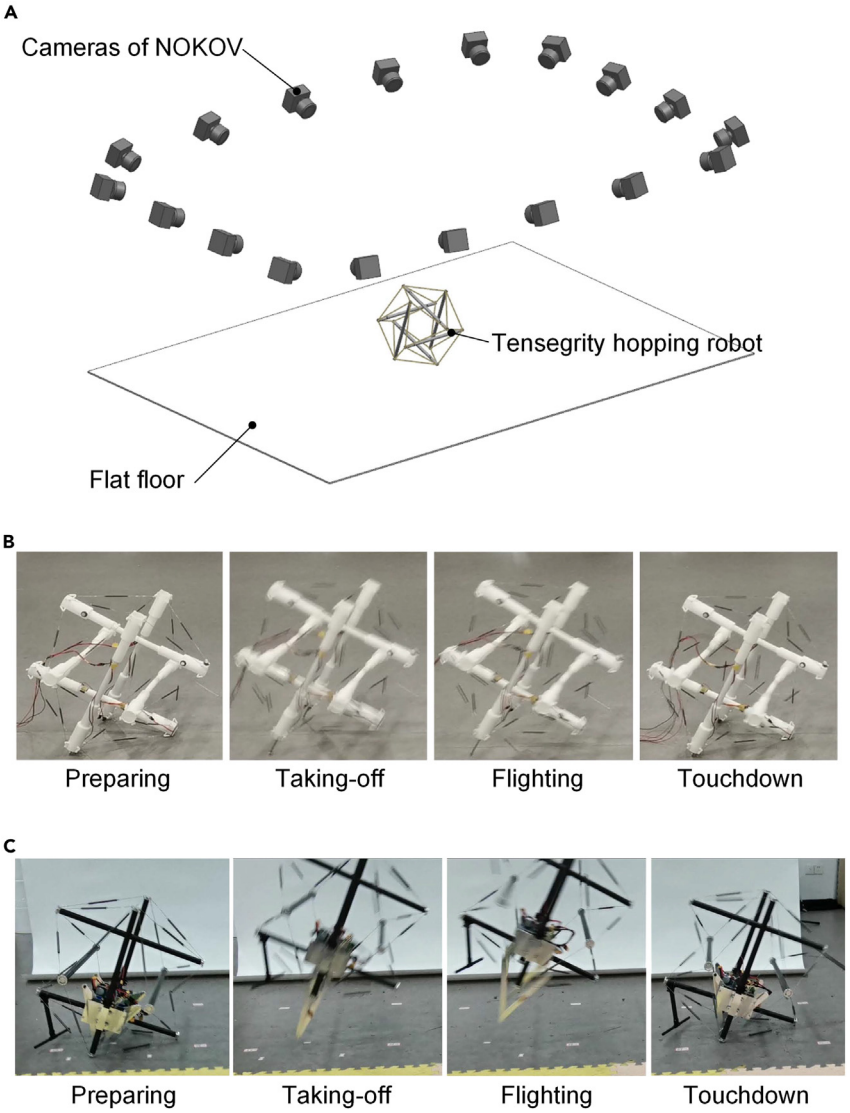

Figure 12. Experimental scene of the proposed robot's hopping experiment

(A) Experimental setup.

(B) Single hopping process of the first robot.

(C) Single hopping process of the second robot.

respectively. In addition, according to Figure 11, the angle between the base triangle's normal vector and the ground's normal vector can always return to zero when a = 0.145 m and a = 0.175 m, which means $\Delta S_{12}S_{22}S_{61}$ or $\Delta S_{12}S_{22}S_{62}$ is always the grounded triangle under these two conditions. Hence, the result of Table 5 and Figure 11 can verify the reasonability of the previous analysis results of the critical value of a.

Hopping experiment

The proposed two tensegrity robots' hopping experiments were conducted to test their hopping and progressing abilities. Both robots' movement processes on flat ground were also recorded by the NOKOV motion capture system with a sampling frequency of 200 Hz. Thus the experimental scene is illustrated in Figure 12.

In the first robot's hopping experiment, it was controlled to progress forward straightly in 10 s with the same driving parameters for both electromagnets. The experimental hopping distance and maximum hopping height in each step with respect to time were plotted in Figure 11A. Then it can be seen from Figure 13A that the average hopping distance is 0.334 m with a standard deviation of 0.022 m and the average hopping height is 0.122 m with a standard deviation of 0.005 m, which shows good stability and reliability for the robot's hopping

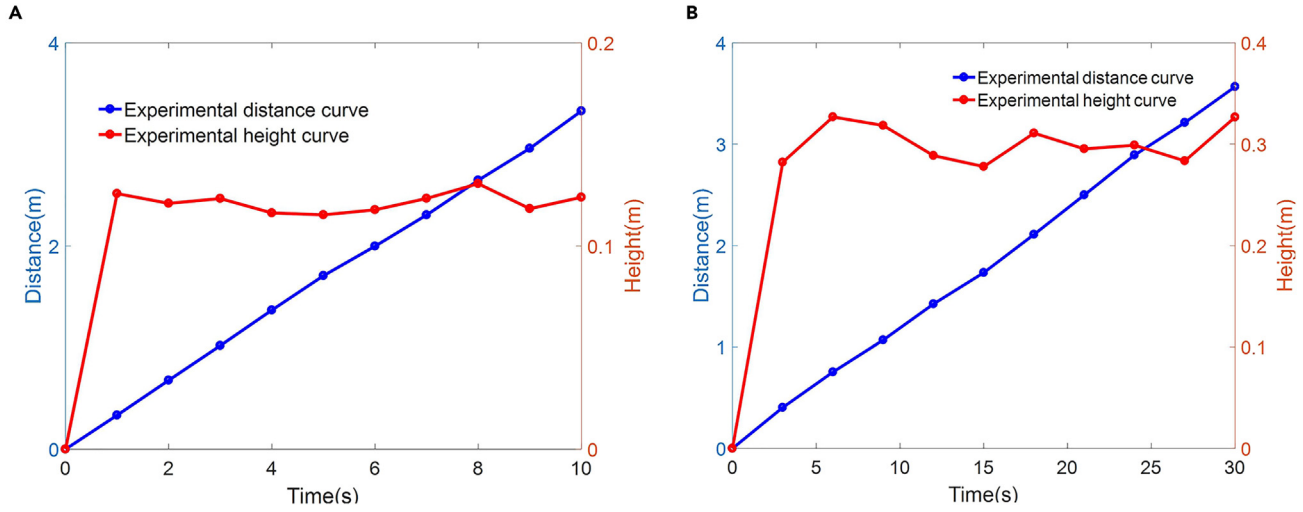

Figure 13. Experimental curves of the proposed robots' hopping processes

(A) Experimental curves of the first robot's hopping process.

(B) Experimental curves of the second robot's hopping process.

action. In addition, the robot's absolute average moving speed and relative moving speed were calculated to be 0.334 m/s and 0.641 body length/s relatively.

Similarly, the second robot was controlled to hop forwards 10 times in 30 s with the same driving parameters for both servo motors. A T-stand is mounted to the robot prototype and used for preventing alternations of contacting ground of the two base triangles. The experimental hopping distance and maximum hopping height in each step with respect to time were presented in Figure 13B. Thus it can be obtained that the robot's average hopping distance is 0.357 m with a standard deviation of 0.032 m and the average hopping height is 0.301 m with a standard deviation of 0.018 m. Additionally, the second robot's absolute average velocity and relative velocity were also determined to be 0.119 m/s and 0.237 body length/s relatively.

According to Figure 13, it is noteworthy that the single hopping periods of the first and second robots were 1 s and 3 s, respectively. Thus the first robot was able to move almost 3 times faster than the second robot. However, the average hopping height of the second robot was 2.5 times higher than that of the first robot. Therefore, most flat terrains were suitable for the first robot while the second robot had more locomotion advantages in tough and unstructured environment.

Table 6 lists the locomotion performance comparison between 10 mobile tensegrity robots and two tensegrity hopping robots proposed in this paper. According to Table 6, the moving speeds of most spherical tensegrity robots with rolling action range between 0.010–0.250 body length/s, and the fastest speed of 0.250 body length/s was achieved by ReC-TeR.[20] Thus it is worth noting that both proposed tensegrity robots have obvious superiority over ReC-TeR or other tensegrity robots in terms of locomotion speed. Especially,

Table 6. Locomotion performance comparison between different tensegrity robots

Robot	Actuation method	Maximum dimension(m)	Total weight (kg)	Max velocity (BL/s)	Max velocity(m/s)
ReC-TeR[20]	DC motors	1.0	1.1	0.250	0.25
SuPERball[11]	BLDC motors	1.7	21.0	0.182	0.40
SuPERball v2[12]	BLDC motors	2.2	38.0	0.186	0.41
TT-2[22]	Linear actuators	0.65	8	0.167	0.107
TT-3[23]	DC motors	0.7	10	0.157	0.110
DuCTT[24]	DC motors	0.415	3.1	0.029	0.012
DuCTT v2[25]	BLDC motors	0.450	3.75	0.031	0.014
LCE based tensegrity robot[26]	Artificial muscles	0.060	0.073	0.019	0.001
Jumping tensegrity robot[21]	SMA springs	0.125	0.121	0.140	0.029
Programmable tensegrity robot[27]	Magnets	0.210	0.169	0.036	0.008
Our first robot	**Electromagnets**	**0.522**	**2.420**	**0.641**	**0.334**
Our second robot	**Servo motor**	**0.503**	**4.210**	**0.237**	**0.119**

the relative average speed of the first proposed robot is nearly 2.5 times larger than that of the second place (ReCTeR). It is worth noting that the jumping tensegrity robot[21] can achieve a maximum sideway jumping height of 0.28 body length and a maximum jumping distance of 0.4 body length. In comparison, the sideway jumping height and jumping distance of the second proposed robot are 0.60 body length and 0.71 body length, respectively. Hence, the jumping performance of the second proposed robot is also better than that of the jumping tensegrity robot.[21]

In summary, the two proposed tensegrity robots have a much larger advantage than traditional tensegrity robots with rolling action in terms of general locomotion ability. More details of the two proposed robots' hopping and progressing movements can also be found in the Video S1.

Conclusion

This paper proposed two kinds of tensegrity hopping robots, which were propelled by push-pull electromagnets or servo motors, respectively. The structural design and working process of both robots were initially illustrated. Then mathematical models for both hopping actuators and the single hopping process were established. The detailed theoretical analysis of the robot's self-righting characteristic was also conducted. Furthermore, the thrust performances of the hopping actuators and the robot's self-righting characteristic were verified by corresponding experiments and simulations. Additionally, in order to validate the locomotion abilities of the robots, the real-world consecutive hopping experiments were conducted. The first robot exhibited an obvious advantage over the second robot in terms of moving speed (0.641 and 0.237 body length/s, respectively). However, the second robot can achieve an average hopping height of 0.301m, which was nearly 2.5 times higher than that of the first one. Then in comparison with other counterparts, the proposed two tensegrity robots surpass the majority of traditional tensegrity rolling robots in terms of locomotion ability, substantiating their larger potential in practical application fields.

Limitations of the study

It is noteworthy that the aerial balance control is indispensable for most hopping robots, as it relates to their consecutive and stable hopping movements.[28] However, the proposed tensegrity hopping robots may not rely on robust control during flight phase necessarily due to their inherent self-righting characteristics. Although both proposed tensegrity hopping robots showed good consecutive hopping abilities, their absolute hopping performances have yet to be improved. Therefore, future research work about the proposed hopping robots will concentrate on the enhancement of the robots' single-hopping capabilities and the combination of various locomotion modes (e.g., combining hopping with rolling or crawling). Thus the proposed robots will be promising in many application scenarios, including space exploration, urban search, military surveillance, environmental detection, etc.

STAR★METHODS

Detailed methods are provided in the online version of this paper and include the following:

- KEY RESOURCES TABLE
- RESOURCE AVAILABILITY
  - Lead contact
  - Materials availability
  - Data and code availability
- METHOD DETAILS
  - Impact model of tensegrity robot's touch-down process
- QUANTIFICATION AND STATISTICAL ANALYSIS

SUPPLEMENTAL INFORMATION

Supplemental information can be found online at https://doi.org/10.1016/j.isci.2024.109226.

ACKNOWLEDGMENTS

This work is mainly supported by National Key Research and Development Program of China (No. 2022YFB4702000).

AUTHOR CONTRIBUTIONS

J. M. conceived the research, designed, and carried out the experiments, and prepared the figures and paper. H. F. and Q. Y. provided support for the experiments, tests, and analysis.

DECLARATION OF INTERESTS

The authors declare no competing interests.

Received: November 14, 2023
Revised: January 2, 2024
Accepted: February 8, 2024
Published: February 16, 2024

REFERENCES

1. Motro, R. (2003). Tensegrity: Structural Systems for the Future (Kogan Page Science).
2. Liu, R., and Yao, Y. (2019). A novel serial–parallel hybrid worm-like robot with multi-mode undulatory locomotion. Mech. Mach. Theor. *137*, 404–431. https://doi.org/10.1016/j.mechmachtheory.2019.03.033.
3. Hu, B., Zhao, J., and Cui, H. (2019). Terminal constraint and mobility analysis of serial-parallel manipulators formed by 3-RPS and 3-SPR PMs. Mech. Mach. Theor. *134*, 685–703. https://doi.org/10.1016/j.mechmachtheory.2019.01.004.
4. Lee, S., and Lee, J. (2014). Form-finding of tensegrity structures with arbitrary strut and cable members. Int. J. Mech. Sci. *85*, 55–62. https://doi.org/10.1016/j.ijmecsci.2014.04.027.
5. Liu, Y., Bi, Q., Yue, X., Wu, J., Yang, B., and Li, Y. (2022). A review on tensegrity structures-based robots. Mech. Mach. Theor. *168*, 104571. https://doi.org/10.1016/j.mechmachtheory.2021.104571.
6. Liu, J., Yu, X., Xu, G., Wang, Z., and Zhang, L. (2023). A unified analytical form-finding of truncated regular octahedral tensegrities. Int. J. Mech. Sci. *239*, 1–15. https://doi.org/10.1016/j.ijmecsci.2022.107857.
7. Paul, C., Valero-Cuevas, F.J., and Lipson, H. (2006). Design and control of tensegrity robots for locomotion. IEEE Trans. Robot. *22*, 944–957. https://doi.org/10.1109/TRO.2006.878980.
8. Webster, V.A., Lonsberry, A.J., Horchler, A.D., Shaw, K.M., Chiel, H.J., and Quinn, R.D. (2013). A segmental mobile robot with active tensegrity bending and noise-driven oscillators. In Paper presented at: 2013 IEEE/ASME International Conference on Advanced Intelligent Mechatronics (IEEE). https://doi.org/10.1109/AIM.2013.6584286.
9. Naribole, S., Anil, R.K., and Chakraborty, G. (2020). Design, mathematical modelling and Analysis of externally actuated somersaulting tensegrity spine. In Paper presented at: 2020 IEEE International Conference on Mechatronics and Robotics Engineering (IEEE). https://doi.org/10.1109/ICMRE49073.2020.9065094.
10. Bruce, J. (2016). Design, Building, Testing, and Control of SUPERball: A Tensegrity Robot to Enable New Forms of Planetary Exploration (Doctoral Dissertation). https://escholarship.org/uc/item/0274v214.
11. Sabelhaus, A.P., Bruce, J., Caluwaerts, K., Manovi, P., Firoozi, R.F., Dobi, S., Agogino, A., and SunSpiral, V. (2015). System design and locomotion of SUPERball, an untethered tensegrity robot. In Paper presented at: 2015 IEEE International Conference on Robotics and Automation (ICRA) (IEEE). https://doi.org/10.1109/ICRA.2015.7139590.
12. Vespignani, M., Friesen, J.M., SunSpiral, V., and Bruce, J. (2018). Design of SUPERball v2, a compliant tensegrity robot for absorbing large impacts. In Paper presented at: 2018 IEEE/RSJ International Conference on Intelligent Robots and Systems (IROS) (IEEE). https://doi.org/10.1109/IROS.2018.8594374.
13. Zhang, M., Geng, X., Bruce, J., Caluwaets, K., Vespignani, M., SunSpiral, V., Abbeel, P., and Levine, S. (2016). Deep reinforcement learning for tensegrity robot locomotion. In Paper presented at: 2016 IEEE International Conference on Robotics and Automation (ICRA) (IEEE). https://doi.org/10.1109/ICRA.2017.7989079.
14. Cera, B., and Agogino, A.M. (2018). Multi-Cable rolling locomotion with spherical tensegrities using model predictive control and deep learning. In Paper presented at: 2018 IEEE/RSJ International Conference on Intelligent Robots and Systems (IROS) (IEEE). https://doi.org/10.1109/IROS.2018.8594401.
15. Raibert, M.H. (1986). Legged Robots that Balance (MIT Press).
16. Mini, B.S.. Boston Dynamics. https://bostondynamics.com.
17. Jung G, P., and Hong, C.C. (2017). Effect of leg compliance in multi-directional jumping of the flea-inspired mechanism. J. Hazard Mater. *153*, 942–947. https://doi.org/10.1088/1748-3190/aa575a.
18. Koh, J.S., Jung, S., and Wood, R.J. (2013). A jumping robotic insect based on a torque reversal catapult mechanism. In Paper presented at: 2013 IEEE/RSJ International Conference on Intelligent Robots and Systems (IROS) (IEEE). https://doi.org/10.1109/IROS.2013.6696899.
19. Zhao, J., Sun, Y., Li, J., Yuan, S., Wang, M., Ding, J., Pu, H., Luo, J., Peng, Y., and Xie, S. (2020). A novel electromagnet-based absolute displacement sensor with approximately linear quasi-zero-stiffness. Int. J. Mech. Sci. *181*, 105695. https://doi.org/10.1016/j.ijmecsci.2020.105695.
20. Bruce, J., Caluwaerts, K., Iscen, A., Sabelhaus, A.P., and SunSpiral, V. (2014). Design and evolution of a modular tensegrity robot platform. In Paper presented at: 2014 IEEE International Conference on Robotics and Automation (ICRA) (IEEE). https://doi.org/10.1109/ICRA.2014.6907361.
21. Chung, Y.S., Lee, J.H., Jang, J.H., Choi, H.R., and Rodrigue, H. (2019). Jumping tensegrity robot based on torsionally prestrained SMA Springs. ACS Appl. Mater. Interfaces *11*, 40793–40799. https://doi.org/10.1021/acsami.9b13062.
22. Kim, K., Agogino, A.K., Toghyan, A., Moon, D., Taneja, L., and Agogino, A.M. (2015). Robust learning of tensegrity robot control for locomotion through form-finding. In Paper presented at: 2013 IEEE/RSJ International Conference on Intelligent Robots and Systems (IROS) (IEEE). https://doi.org/10.1109/IROS.2015.7354204.
23. Chen, L.H., Kim, K., Tang, E., Li, K., House, R., Zhu, E.L., Fountain, K., Agogino, A.M., Agogino, A., Sunspiral, V., and Jung, E. (2017). Soft Spherical tensegrity robot design using rod-centered actuation and control. J. Mech. Robot. *9*, 1–9. https://doi.org/10.1115/1.4036014.
24. Friesen, A., Pogue, J., Bewley, T., Oliveira, M., Skelton, R., and SunSpiral, V. (2014). DuCTT: a tensegrity robot for exploring duct systems. In Paper presented at: 2014 IEEE International Conference on Robotics and Automation (ICRA) (IEEE). https://doi.org/10.1109/ICRA.2014.6907473.
25. Friesen, J.M., Glick, P., Fanton, M., Manovi, P., Xydes, A., Bewley, T., and SunSpiral, V. (2016). The second generation prototype of a duct climbing tensegrity robot, DuCTTv2. In Paper presented at: 2016 IEEE International Conference on Robotics and Automation (ICRA) (IEEE). https://doi.org/10.1109/ICRA.2016.7487361.
26. Wang, Z., Li, K., He, Q., and Cai, S. (2019). A light-powered ultralight tensegrity robot with high deformability and load capacity. Adv. Mater. *31*, e18068499. https://doi.org/10.1002/adma.201806849.
27. Lee, H., Jang, Y., Choe, J.K., Lee, S., Song, H., Lee, J.P., Lone, N., and Kim, J. (2020). 3D-printed programmable tensegrity for soft robotics. Sci. Robot. *5*, eaay9024-12. https://doi.org/10.1126/scirobotics.aay9024.
28. Souza, G.N., Oliveira, T.R., and Leite, A.C. (2021). Robust control design for a hopping robot in flight phase using the sliding mode approach. In Paper presented at: 2021 IEEE International Conference on Automation Science and Engineering (CASE) (IEEE), pp. 1060–1066. https://doi.org/10.1109/CASE49439.2021.9551560.
29. Stronge, W.J. (2018). Impact mechanics (Cambridge university press).

STAR★METHODS

KEY RESOURCES TABLE

REAGENT or RESOURCE	SOURCE	IDENTIFIER
Chemicals, peptides, and recombinant proteins		
Synthetic resin	Wenext office flagship store (Taobao, China)	N/A
6061 aluminum alloy	Sogaworks (Taobao, China)	N/A
Carbon fiber	Shanmeibang store (Taobao, China)	N/A
Software and algorithms		
MATLAB	Mathworks, Inc.	N/A
Unigraphics NX	Siemens PLM Software	N/A
ideaMaker	Raise 3D Technologies, Inc.	N/A
Arduino IDE	Arduino LCC	N/A

RESOURCE AVAILABILITY

Lead contact

Further information and requests for resources and reagents should be directed to and will be fulfilled by the lead contact, Hao Fang (E-mail: fangh@bit.edu.cn).

Materials availability

This study did not generate new materials. Materials used in the study are commercially available.

Data and code availability

- All data reported in this paper will be shared by the lead contact upon reasonable request.
- No new code was generated during the course of this study.
- Any additional information required to reanalyze the data reported in this paper is available from the lead contact upon reasonable request.

METHOD DETAILS

Impact model of tensegrity robot's touch-down process

Although the tensegrity robot has good performance of shock-absorbing, it is still necessary to model the free-falling robot's impact force upon ground contact for better structural stability of the robot. Thus it can be assumed that the robot would not decrease the impact load by active deformation and robot is approximately treated as a regular spherical structure. In terms of the robot's impact process with ground, it can be obtained according to the theorem of momentum that

$$\int_0^{\Delta t} F_n(t)\mathrm{d}t - \int_0^{\Delta t} M\boldsymbol{g}\mathrm{d}t = M\boldsymbol{v}_{n0} + M\boldsymbol{v}_{n1} \quad \text{(Equation 21)}$$

where $\boldsymbol{F}_n(t)$ is the impact force from ground and Δt is the impact duration. $\boldsymbol{v}_{n0} = \boldsymbol{v}_0 \sin\theta$ is the normal velocity of the robot before impact and θ is the robot's velocity angle with respect to the ground; $\boldsymbol{v}_{n1} = e_n \boldsymbol{v}_{n0}$ is the normal velocity of the robot after impact where $e_n \in [0, 1]$ is the coefficient of restitution.

Then the maximum impact force of $\boldsymbol{F}_{n\max}$ can be calculated by

$$\boldsymbol{F}_{n\,\max} = k_i \overline{\boldsymbol{F}}_n \quad \text{(Equation 22)}$$

where k_i is the amplification coefficient.[29]

According to (21), the average impact force of $\overline{\boldsymbol{F}}_n$ can be obtained as

$$\overline{\boldsymbol{F}}_n = M\boldsymbol{g} + \frac{M\boldsymbol{v}_0 \sin\theta(1+e_n)}{\Delta t} \quad \text{(Equation 23)}$$

In addition, the robot's horizontal velocity component can also make it suffer from sliding friction force on ground, that is

$$\begin{cases} \overline{F}_r = \mu \overline{F}_n = \mu \left[Mg + \dfrac{Mv_0 \sin\theta(1+e_n)}{\Delta t} \right] \\ F_{r\,\max} = \mu F_{n\,\max} = \mu k_i \left[Mg + \dfrac{Mv_0 \sin\theta(1+e_n)}{\Delta t} \right] \end{cases} \quad \text{(Equation 24)}$$

where μ is the coefficient of sliding friction of the ground.

So the amplitude of the impact force suffered by the robot is

$$P_{\max} = k_i \sqrt{1+\mu^2} \left[Mg + \frac{Mv_0 \sin\theta(1+e_n)}{\Delta t} \right] \quad \text{(Equation 25)}$$

The amplification coefficient k_i and impact duration Δt can be calculated by related theories of elastic mechanics.[29] The amplification coefficient k_i is the function of coefficient of restitution e_n, that is:

$$k_i = \frac{F_{n\,\max}}{\overline{F}_n} = \frac{1.84\left(1+\dfrac{1}{e_n^{0.2}}\right)}{1+e_n} \quad \text{(Equation 26)}$$

The impact duration Δt can be obtained by:

$$\Delta t = 1.47 \left(\frac{5M}{4n} \right)^{0.2} \left[\frac{1}{v_{n0}^{0.2}} + \frac{1}{(e_n v_{n0})^{0.2}} \right] \quad \text{(Equation 27)}$$

where n is a constant related to the characteristics of two colliding objects. Its calculation formula is as follows:

$$n = \frac{4E_1 E_G}{3\left(E_1+E_G - \nu_1^2 E_G - \nu_G^2 E_1\right)} \sqrt{\frac{R_1 R_G}{R_1+R_G}} \quad \text{(Equation 28)}$$

where E_1, E_G, ν_1, ν_G, R_1, R_G are the elasticity moduli, Poisson's ratios and equivalent radii of the tensegrity robot and ground respectively. As the equivalent radius of the ground R_G is larger than of the tensegrity robot R_1, thus (Equation 28) can be simplified as:

$$n = \frac{4E_1 E_G}{3\left(E_1+E_G - \nu_1^2 E_G - \nu_G^2 E_1\right)} \sqrt{R_1} \quad \text{(Equation 29)}$$

Therefore the impact duration Δt can be solved by substituting (Equation 29) into (Equation 27), and the amplitude of the impact force suffered by the robot can be determined by substituting the values of k_i and Δt into (Equation 25). This mathematic model of impact force can provide a theoretical basis for reliable structural design of the tensegrity robot.

QUANTIFICATION AND STATISTICAL ANALYSIS

The raw experimental data in the part of results and discussion was measured by a 3-D motion capture system (NOKOV, China) with a sampling frequency of 200 Hz. Figures were produced by MATLAB 2016 from the raw data.